Quantitative magnetic resonance mapping of the myelin bilayer reflects pathology in multiple sclerosis brain tissue

Baadsvik, Emily Louise ; Weiger, Markus ; Froidevaux, Romain ; Faigle, Wolfgang ; Ineichen, Benjamin V ; Pruessmann, Klaas P

DOI: https://doi.org/10.1126/sciadv.adi0611

DISEASES AND DISORDERS

Quantitative magnetic resonance mapping of the myelin bilayer reflects pathology in multiple sclerosis brain tissue

Emily Louise Baadsvik[1], Markus Weiger[1]*, Romain Froidevaux[1], Wolfgang Faigle[2,3], Benjamin V. Ineichen[4,5]†, Klaas P. Pruessmann[1]†

Multiple sclerosis (MS) is a neuroinflammatory disease characterized by loss of myelin (demyelination) and, to a certain extent, subsequent myelin repair (remyelination). To better understand the pathomechanisms underlying de- and remyelination and to monitor the efficacy of treatments aimed at regenerating myelin, techniques offering noninvasive visualizations of myelin are warranted. Magnetic resonance (MR) imaging has long been at the forefront of efforts to visualize myelin, but it has only recently become feasible to access the rapidly decaying resonance signals stemming from the myelin lipid-protein bilayer itself. Here, we show that direct MR mapping of the bilayer yields highly specific myelin maps in brain tissue from patients with MS. Furthermore, examination of the bilayer signal behavior is found to reveal pathological alterations in normal-appearing white and gray matter. These results indicate promise for in vivo implementations of the myelin bilayer mapping technique, with prospective applications in basic research, diagnostics, disease monitoring, and drug development.

INTRODUCTION

Multiple sclerosis (MS) is the most common neuroinflammatory disease, with more than 2.8 million cases reported worldwide (*1*), and is a leading cause of nontraumatic disability in young adults. The pathological hallmark of MS is focal areas of inflammatory myelin loss (demyelination) referred to as MS lesions or plaques, which can undergo subsequent myelin repair (remyelination) (*2*).

Treatment prospects for patients with MS have improved tremendously in recent years, with a large battery of disease-modifying treatments now available (*3*, *4*). However, a critical shortcoming in the therapy of MS is the later disease stage, in which patients suffer from incremental neurological disability. Although the underlying pathomechanisms are not fully understood, it is clear that chronic demyelination and subsequent neurodegeneration are key drivers for the progressive clinical phenotype (*5*). Notably, it has been shown that pharmacologically fostering remyelination mitigates neuroaxonal damage in patients with MS (*6*).

Magnetic resonance imaging (MRI) has emerged as an important tool to support diagnostic workup of suspected MS cases and monitor treatment response (*7*, *8*). However, clinical MRI suffers from low specificity for the underlying tissue signature (*9*), meaning that it is difficult to infer tissue pathology based on the image contrast. Therefore, to understand the mechanisms behind demyelination and myelin repair, as well as evaluate the efficacy of putative remyelinating candidates, there is a demand for techniques offering noninvasive, specific visualization of myelin.

Myelin in the central nervous system (CNS) is a tightly compacted extension of the plasma membrane of oligodendrocytes that is wrapped concentrically around axons, facilitating efficient transmission of neuronal impulses (*10*). The lipid-protein bilayers of the compacted membrane have a characteristic, lipid-rich (70% of dry weight) composition (*11*, *12*). The myelin sheath additionally contains pools of intra- and extracellular water, collectively referred to as myelin water, that are trapped between the layers of membrane.

Typically, MRI techniques target resonance signals from protons (^{1}H) because of their abundance in biological tissues. Because of differences in their chemical environments, the signals from aqueous protons have much longer lifetimes [characterized by the transverse decay constant (T_2)] than the signals from nonaqueous protons. Water signals exhibit T_2′s from tens of milliseconds [for myelin water (*13*)] to several seconds, while signals from protons in the myelin bilayer exhibit a spectrum of T_2′s covering primarily the tens to hundreds of microseconds range (*14*). Standard MRI systems are not capable of detecting the rapidly decaying signals from the myelin bilayer; however, dedicated short-T_2 imaging hardware and methodology (*15*) enable access to the majority of myelin bilayer signals (*16*).

The myelin bilayer is not the only source of nonaqueous proton signals in the CNS. Obtaining maps specific for the myelin bilayer, therefore, relies not only on sensitivity to nonaqueous signals but also on the ability to separate myelin bilayer signals from nonmyelin nonaqueous signals. The unique structure of the myelin bilayer compared with other cellular content in the CNS results in characteristic decay behavior that can be exploited to isolate signal contributions stemming from the myelin bilayer. Similarly, aqueous content can be separated from nonaqueous content through differences in decay properties.

In previous work, we developed a technique for mapping the myelin bilayer that uses a model fitting procedure for signal component separation (*16*), which demonstrated robust and promising performance in nonpathological human brain ex vivo (*17*). In the present study, we show that this technique is sensitive to myelin pathology, producing maps of myelin content in brain tissue from MS

[1]Institute for Biomedical Engineering, ETH Zurich and University of Zurich, Zurich, Switzerland. [2]Neuroimmunology and MS Research Section, Neurology Clinic, University of Zurich, University Hospital Zurich, Zurich, Switzerland. [3]Institut Curie, Immunity and Cancer Unit 932, Paris, France. [4]Department of Neuroradiology, Clinical Neuroscience Center, University Hospital Zurich, University of Zurich, Zurich, Switzerland. [5]Center for Reproducible Science, University of Zurich, Zurich, Switzerland.
*Corresponding author. Email: weiger@biomed.ee.ethz.ch
†These authors contributed equally to this work.

donors that closely reflect myelin histopathological findings. In addition, we uncover interesting indications of tissue alterations in normal-appearing white and gray matter (NAWM and NAGM, respectively) through examination of resonance signal behavior.

RESULTS

Characteristics of included MS cases/samples

To cover a variety of disease manifestations, we examined nine brain tissue samples from six MS donors. Table 1 provides detailed donor information and an overview of the samples. All donors suffered from a progressive clinical MS phenotype, and their median age was 48 years (range, 39 to 58 years).

Up to two tissue samples were included per donor. Six samples were subjected to a D_2O exchange, a process that replaces the protons of water molecules with deuterons (^2D) and thereby effectively renders aqueous content invisible with proton MRI (*14*, *16*). Samples subjected to D_2O exchange are termed D_2O samples, and samples not subjected to D_2O exchange are termed H_2O samples.

Myelin bilayer maps in MS brain samples show good correspondence with myelin histopathology and macroscopic sample anatomy

The myelin specificity of the employed myelin bilayer mapping technique was assessed through qualitative comparison and quantitative correlation with myelin histopathological stains. Myelin bilayer maps of the samples, which formally portray voxel-wise fitted amplitudes of the nonaqueous signal component with ultrashort decay constant (A_U; see Materials and Methods), are presented in Fig. 1 alongside sample cryosections treated with immunohistochemistry for myelin oligodendrocyte glycoprotein (MOG) or luxol fast blue (LFB) myelin staining. Visual photographs from both sides of the samples, as well as high-resolution short-T_2 MRI images depicting all (nonaqueous and aqueous) signal components, are presented for anatomical reference.

In the myelin bilayer maps, NAWM [i.e., the macroscopically normal-appearing yet disease-affected white matter (WM)] exhibits the highest amplitudes. NAGM exhibits low but nonzero amplitudes. In and adjacent to MS lesions, amplitudes are variable, with some lesions exhibiting practically zero amplitude (i.e., completely demyelinated; see, e.g., sample A1) and others exhibiting intermediate amplitude (i.e., partially de- or remyelinated; see, e.g., sample C1). The staining intensity seen for both MOG- and LFB-processed sections corresponds well with the contrast observed in the myelin bilayer maps, indicating good specificity for myelin.

For the H_2O samples, the high-resolution reference images show contributions from water signals both within the samples and in the sample container, which, depending on the sample, was filled with either D_2O or H_2O saline solution. The quality of the myelin bilayer maps for the H_2O samples is slightly inferior to that achieved for the D_2O samples because the nonaqueous signal components are harder to separate in the presence of dominant water signals. However, the performance of the myelin bilayer mapping procedure in H_2O samples is sufficient for robust employment also in pathological tissue with native water content, which supports future in vivo application of the technique.

Because MOG is a myelin-specific protein, the staining intensity obtained from MOG immunohistochemistry can be considered an adequate proxy for myelin content. To formally assess the myelin specificity of our myelin bilayer mapping technique, linear correlation analysis (see Materials and Methods) between the image intensities in the myelin bilayer map and the MOG stain for sample A1 was performed; the results are presented in Fig. 2, and the underlying data can be found in table S1. The correlation is strong [correlation coefficient (r) = 0.94, $P < 0.001$], verifying that the myelin bilayer maps are highly specific for myelin. The different tissue types form discrete clusters with a reasonable intensity distribution.

Extended perspectives on the model fitting procedure validate the reliability of the myelin bilayer maps

The performance of the employed myelin bilayer mapping technique was investigated by examining the parameters of the signal model that were fitted simultaneously with the amplitude of the ultrashort (myelin bilayer) signal component (see Materials and Methods). Figure 3 displays maps for two representative D_2O samples of the amplitude of the myelin bilayer component, the amplitude of the nonaqueous signal component with short decay constant (A_S) representing residual nonaqueous content, the amplitude

Table 1. MS donor and sample information. NA, not available.

Donor	A	B	C	D	E	F
Age (years)	51	58	45	42	39	50
Sex	Male	Male	Female	Male	Female	Male
Cause of death	Respiratory failure	Chest infection/MS	Pneumonia/MS	Pneumonia/MS	Broncho-pneumonia/MS	MS
MS classification	Secondary progressive	Secondary progressive	Secondary progressive	Secondary progressive	Primary progressive	Secondary progressive
Disease duration (years)	18	NA	25	21	13	29
Diagnosis duration (years)	15	13	22	21	9	28
Postmortem interval (hours)	17	25	17	15	9	8
Samples	A1 (D_2O)	B1 (D_2O)	C1 (D_2O)	D1 (D_2O), D2 (D_2O)	E1 (D_2O), E2 (H_2O)	F1 (H_2O), F2 (H_2O)

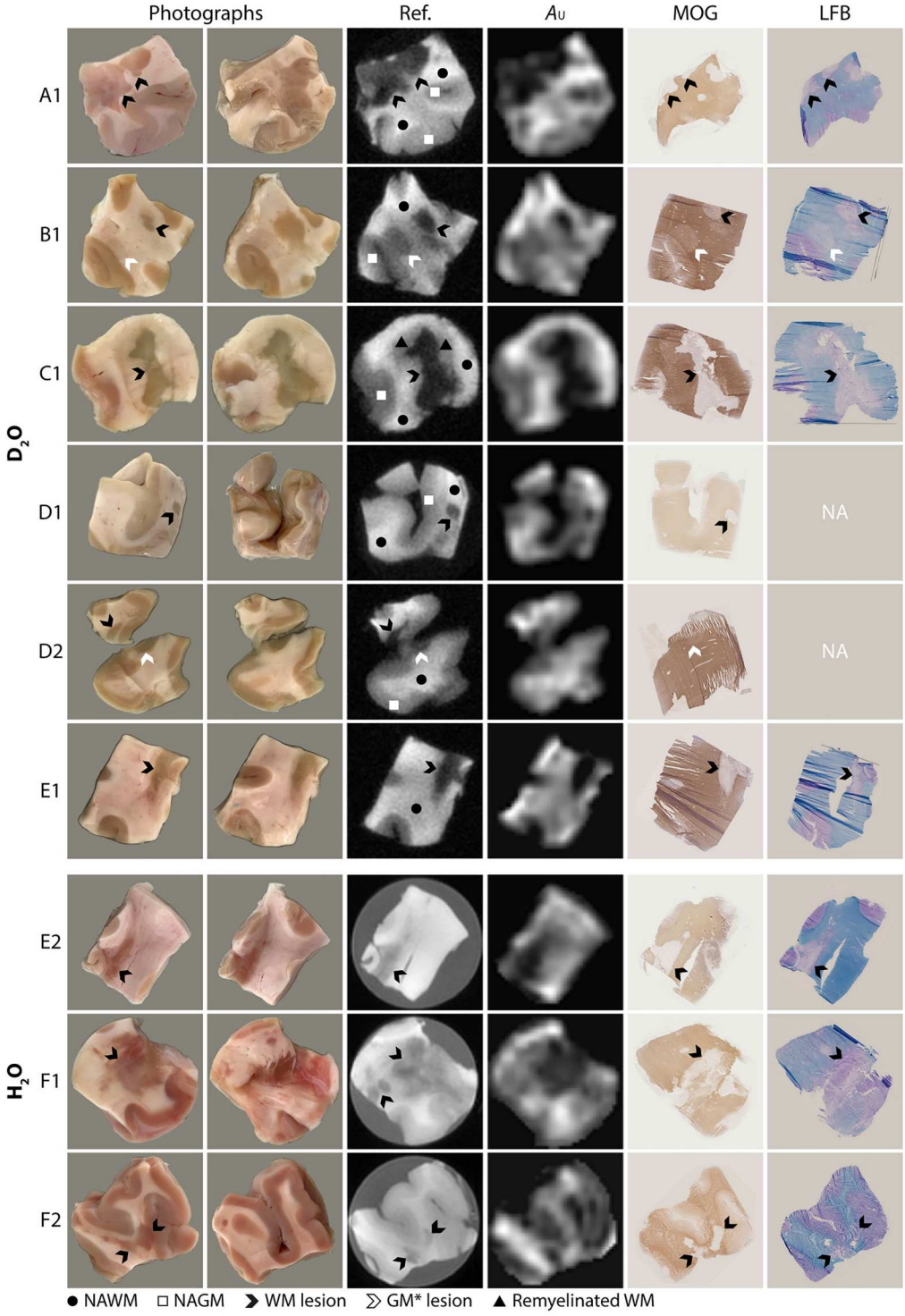

Fig. 1. Myelin bilayer maps of MS tissue enabled by short-T_2 MRI. Depicted are sample photographs (both sides), high-resolution short-T_2 MRI reference images (Ref.), amplitude maps of the ultrashort signal component representing the myelin bilayer (A_U), cryosections treated with myelin oligodendrocyte glycoprotein (MOG) immunohistochemistry, and cryosections treated with luxol fast blue (LFB) myelin staining. Note that LFB stains are not available (NA) in samples D1 and D2 (see Materials and Methods). Locations of white matter (WM) or gray matter (GM) MS lesions are indicated by arrowheads, and regions of normal-appearing white matter (NAWM), normal-appearing gray matter (NAGM), or remyelinated WM used for detailed signal analysis are marked. Because of the thickness of the samples and the resolution of the MRI images, some topological sample features vary slightly between the photographs, MRI slices, and cryosections of a given sample. Folding, tearing, and/or freezing artifacts can be observed in some of the cryosections. *GM or WM/GM lesion.

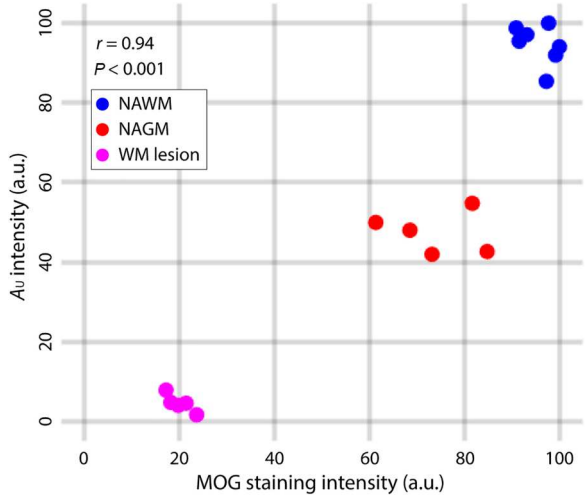

Fig. 2. Linear correlations between the image intensities in the myelin bilayer map and the MOG stain for sample A1. A strong correlation is found between the amplitude map of the ultrashort signal component representing the myelin bilayer (A_U) and the cryosection treated with immunohistochemistry for MOG (r = 0.94, P < 0.001). Data were collected from NAWM, NAGM, or the WM lesion. a.u., arbitrary units.

of the aqueous signal component with relatively long decay constant (A_W) representing water content, the parameter representing the local resonance frequency offset (Δf), and the fit residual (squared 2-norm) quantifying the goodness of fit.

Compared to the myelin bilayer component, the amplitudes of the residual nonaqueous component show less contrast between tissue types, resulting in overall higher signal homogeneity. Amplitudes across MS lesions are variable also for the residual nonaqueous component but are relatively higher compared to surrounding tissue than for the myelin bilayer component. The amplitudes of the water component are largely uniform, but slight contrast is present, attributed to some T_1 weighting in the underlying data (*17*).

The maps of the local resonance frequency offset are mostly smooth and within a reasonable range. However, for sample B1, there is a discrepancy in the lower right corner of the map, which is attributed to susceptibility gradients related to the sharp edges of the sample (which cause an abrupt transition from surrounding D_2O solution to tissue). The susceptibility gradients lead to intravoxel dephasing, resulting in signal dropout in the amplitude maps of the residual nonaqueous and water components because the dephasing has more impact on longer-lived signals, leading to misinterpretation of signals from these components as shorter-lived myelin bilayer signals.

The maps of the normalized fit residuals show generally good fit performance (i.e., low values) in the interior of the samples. The residuals are elevated around the sample edges, reflecting primarily partial volume effects. Locations of MS lesions generally exhibit only slightly elevated fit residuals, although there are a few regions within MS lesions where the residuals are substantially elevated, which is likely due to insufficient signal-to-noise ratio or breakdown of the signal model.

Overall, the maps presented in Fig. 3 are of good quality and display a reasonable contrast and behavior, demonstrating robust performance of the fitting procedure also in tissue exhibiting pathological alterations.

The signal components exhibit prolonged decay constants in NAWM and NAGM compared to those in nonpathological counterparts

The isolation of nonaqueous signals achieved through D_2O exchange enables analysis of the behavior of the nonaqueous signal components, which was exploited to investigate tissue alterations as a result of MS pathology. The regions of interest (ROIs) marked in Fig. 1 were examined, and, to stabilize the fits with respect to noise and potential local signal variations, signals from multiple voxels in each ROI were averaged before fitting. In addition to fits yielding the amplitudes of the signal components, separate fits designed to reveal the super-exponential decay constants ($T_{2,\mathrm{min}}$) of the nonaqueous components were used (see Materials and Methods); the results are presented in Table 2. Equivalent results presented for nonpathological human WM and gray matter (GM) in what we will hereby refer to as the reference study (*17*) are also provided in Table 2 for comparison.

The amplitudes are normalized to give the relative contribution of each component to the total nonaqueous signal. For NAWM and NAGM, the means and SDs over all the ROIs indicated in Fig. 1 are provided; results for individual ROIs are listed in table S2. For features related to MS pathology, results are presented separately for each examined ROI. The MS lesions in samples D2 and E1 were not included for analysis because these samples are particularly affected by susceptibility and partial volume effects; for the same reason, no NAGM areas in sample E1 were analyzed.

The nonaqueous component amplitudes found for NAWM and NAGM are comparable to those reported for nonpathological WM and GM in the reference study (*17*). In contrast, the decay constants found for the MS samples are longer than those reported for the nonpathological samples.

In and around MS lesions, the nonaqueous component amplitudes and decay constants are more homogeneous than the variations in visual presentation would suggest, indicating a similar tissue signature across all examined lesions. The amplitude relationship between the two nonaqueous components is largely the same as that found in NAWM, except for the lesion in sample A1, which exhibits a higher proportion of residual nonaqueous content. The decay constants of the myelin bilayer component are generally similar to those found in NAGM but exhibit slightly larger variations. Notable variations across MS features are found only in the decay constants of the residual nonaqueous component, but, because of low signal-to-noise ratio of this component in MS lesions, these fitted values are not considered to be informative.

Amplitude normalization yields quantitative myelin bilayer maps

In MRI, the absolute voxel values are usually not instructive because they are affected by various factors such as receiver gain settings or radiofrequency coil sensitivity and loading. Consequently, the fitted component amplitudes are not directly comparable across different samples or different scan sessions of the same sample. To produce quantitative myelin maps, that is, maps in which the amplitude values reflect myelin content, the fitted component amplitudes were therefore normalized.

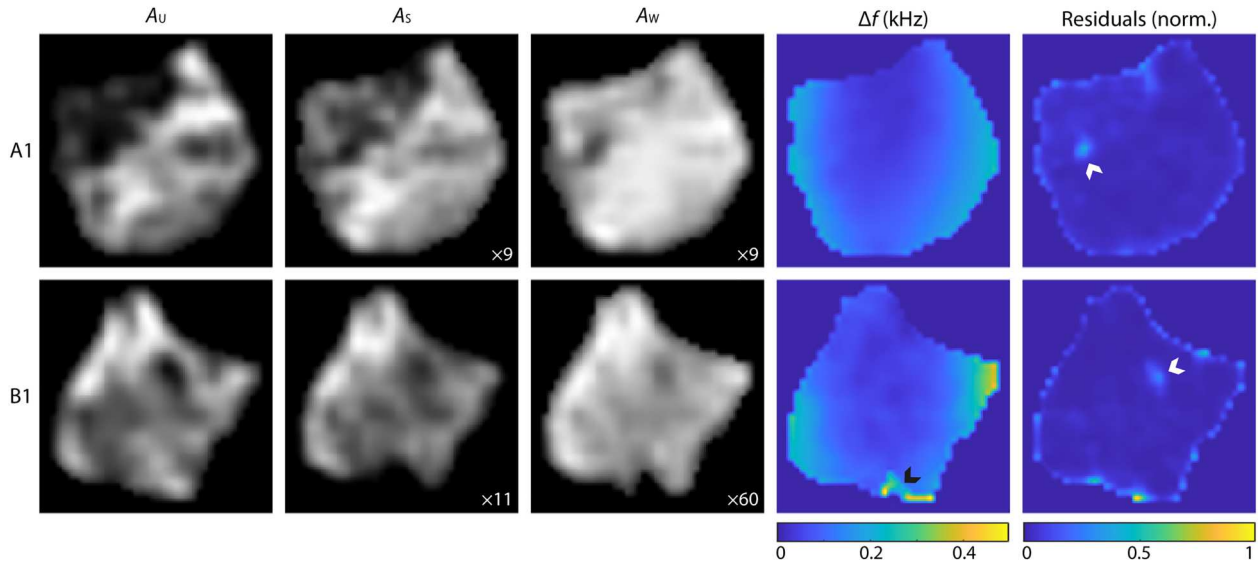

Fig. 3. Maps of the three components included in the signal model. Depicted are maps of the amplitudes of the ultrashort signal component representing the myelin bilayer (A_U), the short signal component representing residual nonaqueous content (A_S), and the water component (A_W), as well as maps of the local resonance frequency offset (Δf) and fit residuals for two representative D_2O samples (A1 and B1). The A_S and A_W maps are scaled in relation to the A_U map of the respective sample; the scaling factors are written in the lower right-hand corners of the maps. For sample B1, susceptibility effects materialized in Δf (location indicated by black arrowhead) lead to signal dropout in the A_S and A_W maps. The fit residuals are normalized by the maximum residual across the two samples and are generally slightly elevated around the edges of the samples and in MS lesions. Certain locations (indicated by white arrowheads) within MS lesions exhibit particularly large fit residuals, which could indicate insufficient signal-to-noise ratio or breakdown of the signal model.

Table 2. Signal analysis results for various ROIs in the D_2O samples. For NAWM and NAGM, the means and SDs over all regions marked in Fig. 1 are given (note that the markers only indicate the tissue; they are not intended to outline the full ROI). For MS features, results for selected regions are reported individually (descriptions refer to markers in Fig. 1). The component amplitudes and decay constants are determined using separate fitting procedures. The mean values for WM and GM reported in the reference study (*17*) for nonpathological D_2O samples are also provided.

		$A_U/(A_U + A_S)$	$A_S/(A_U + A_S)$	$T_{2,min,U}$ (μs)	$T_{2,min,S}$ (μs)
NAWM	Mean	0.91	0.09	8.1	197
	SD	0.01	0.01	1.3	75
NAGM	Mean	0.86	0.14	12.3	340
	SD	0.05	0.05	1.7	101
MS features					
Sample	Description				
A1	WM lesion (right part)	0.75	0.25	10.4	1000†
A1	WM lesion (left part)	0.71	0.29	14.2	402
B1	WM lesion	0.89	0.11	14.5	432
B1	GM* lesion	0.92	0.08	12.5	230
C1	Remyelinated WM (right)	0.93	0.07	10.6	622
C1	Remyelinated WM (left)	0.91	0.09	14.2	982
C1	WM lesion	0.89	0.11	11.1	1000†
D1	WM lesion	0.87	0.13	8.2	377
Nonpathological reference (*17*)					
WM	Mean	0.91	0.09	5.5	102
GM	Mean	0.83	0.17	9.4	171

*WM lesion believed to spread into GM, but only WM voxels are used in the analysis. †Upper limit of parameter value.

The component amplitudes provided in Table 2 follow the normalization strategy proposed in the reference study (*17*), which was designed primarily for comparisons of relative signal contributions in different samples. However, these relative component amplitudes do not capture the intrasample variations, particularly in relation to MS pathology, seen in the myelin bilayer maps in Fig. 1. For comparisons of different locations within the same sample, we propose a strategy in which the amplitudes of each signal component are normalized by the mean amplitude of the respective component in a reference NAWM region.

Myelin bilayer maps normalized according to the proposed strategy are shown in Fig. 4 for the four samples whose MS features were analyzed in Table 2. The contrast in the normalized maps is the same as in the original maps (see Fig. 1) and is reflected well in the amplitude values. NAGM exhibits between 30 and 50% of the amplitude of NAWM. Certain MS lesions yield almost negligible myelin amplitudes (see, e.g., the lesions in sample A1), while others yield similar myelin amplitudes to NAGM (see, e.g., the WM/GM lesion in sample B1). The partly remyelinated WM regions in sample C1 also yield similar amplitudes to NAGM.

Some variations in the normalized amplitudes across different regions of the same tissue type within a given sample are observed (see, e.g., the NAWM regions in sample C1). Such variations could reflect several factors, such as the radiofrequency coil sensitivity, partial volume effects, or actual tissue differences. Variations in the normalized amplitudes across regions of the same tissue type in different samples are also present (see, for instance, the NAGM regions in samples A1 and C1) and are most likely caused by the reference NAWM regions not being entirely reliable in these rather small and heterogeneous samples. For sample D1, the normalized amplitude in the MS lesion is higher compared to that in the NAGM region than expected from visual inspection, which reflects partial volume effects in the ROI.

DISCUSSION

In this study, an emerging short-T_2 MRI technique for mapping the myelin bilayer was exploited to gain insights into pathological changes in brain tissue from MS donors. By separating the two nonaqueous signal components, the technique provided high specificity for myelin. Detailed signal analysis enabled by D_2O exchange in given samples revealed changes in NAWM and NAGM compared to nonpathological counterparts (*17*) in the form of prolonged decay constants. Normalization of the myelin bilayer maps by a reference NAWM region permitted quantification of myelin content, thereby facilitating comparisons of myelin content at different locations within the samples. The employed myelin bilayer mapping technique showed robust behavior for the case of pathological tissue changes, also in samples with native water content.

The prolonged decay constants found in NAWM and NAGM compared to in nonpathological counterparts (*17*) are in line with the notion that MS pathology is widespread in the CNS rather than limited to focal lesions (*18*). Furthermore, because the tightly compacted structure of the myelin bilayer is the main reason why its decay constants are shorter than those associated with nonmyelin nonaqueous CNS content, it is reasonable to consider prolonged decay constants of the myelin bilayer component as an indication of compromised myelin integrity. For the residual nonaqueous component, the changes in decay constants between MS and nonpathological brain tissue could indicate different cellular microenvironments within the CNS present in MS, for instance, accumulation of immune cells within the parenchyma, activation of microglia cells, and/or neuroaxonal degeneration.

In addition to enabling comparisons of amplitudes within the myelin bilayer map of a given sample, the normalization strategy used in Fig. 4 should allow comparisons across different scan sessions of the same sample provided that the reference NAWM region does not undergo substantial changes between scan sessions. This would render the normalization strategy suitable for longitudinal monitoring of myelin content in vivo.

The signal model underlying the myelin bilayer mapping procedure was designed on the basis of signal behavior seen in nonpathological WM. Employment of this signal model in pathological tissue, therefore, relies on the assumption that the pathological changes affect only the amplitudes of the signal components, not the components themselves. As seen in Table 2, this condition is not entirely true for MS tissue. However, the differences between the decay constants found in MS and nonpathological brain tissue are expected to have little impact on the component amplitude maps, as concluded in the reference study (*17*) for the similar situation of fitting GM signals using WM components; the three signal

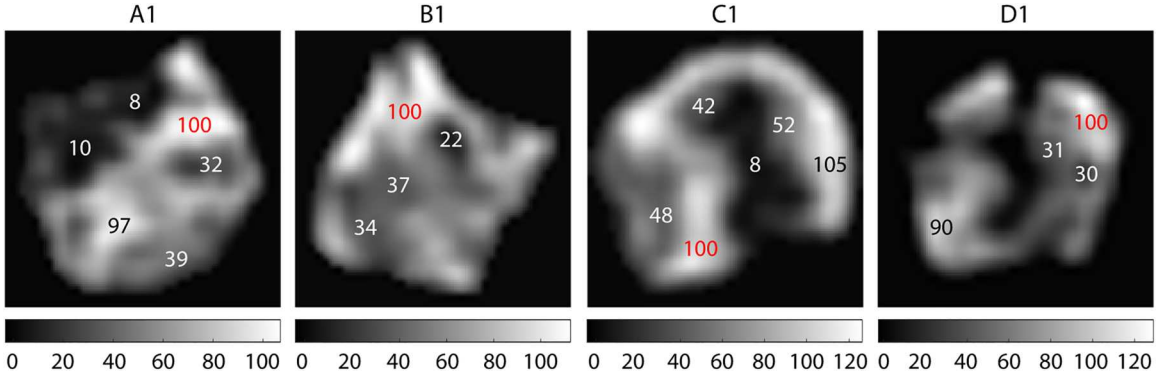

Fig. 4. Normalized myelin bilayer maps. Amplitude maps of the ultrashort signal component representing the myelin bilayer normalized by the mean amplitude in a reference NAWM region for the four samples analyzed in detail in Table 2. The mean normalized amplitudes in the ROIs marked in Fig. 1 are written in corresponding locations, and the red value marks the region used for the normalization in each sample.

components are still distinct from each other, and, thus, their contributions are unlikely to be misallocated during fitting.

Analysis of resonance signals is regularly performed using nuclear magnetic resonance (NMR) spectroscopic methods without spatial localization, which avoid the complications of spatial encoding necessary for imaging but commonly involve sample destruction as part of experiment preparation. Several NMR studies have been performed on myelin bilayer signals (*14*, *19*–*21*), and their insights have been key to developing and validating the signal model employed here. That said, as evidenced by the present and reference studies (*17*), signal analysis applied to individual imaging voxels can provide useful information of a similar nature to NMR studies without compromising the samples, enabling additional studies such as histopathology to be performed on the same samples.

Along with the decay constants, the signal components are also characterized by their chemical shifts. However, it was found in the reference study (*17*) that component chemical shifts are often not particularly informative due to inherent limitations of the signal analysis procedure. Therefore, component chemical shifts fitted along with component decay constants were not further considered or reported in this study.

The brain samples used in this study were frozen after tissue retrieval. Minor changes in tissue water content and in the amplitude ratio of the two nonaqueous components have been observed as a result of frozen storage, but these effects occur primarily for H_2O samples (*17*). Because signal analysis was only performed in D_2O samples in the present study, we do not anticipate any relevant impact on our MRI results from the frozen sample storage. It is possible that freezing tissue affects the processes involved in histopathology; however, no visual differences were observed in the reference study (*17*) between stains for tissue samples that had undergone frozen storage and tissue samples fresh from autopsy.

Image resolution presents a limit to the size of features, most notably MS lesions, that can be detected and examined with the employed myelin bilayer mapping technique. Although the quality of the myelin bilayer maps presented in Fig. 1 is comparable to that achieved for the nonpathological human brain samples in the reference study (*17*), some of the features of interest seen in the high-resolution reference images do not cover entire voxels in the myelin bilayer maps and, thus, are subject to partial volume effects. Partial volume effects effectively limit the size of features for which ROI analysis can be instructive, as evidenced by the bias observed in the normalized myelin bilayer amplitude for the MS lesion in sample D1 (see Fig. 4).

The MS lesion in sample C1 is considered to be partly remyelinated (see markers in Fig. 1). That said, the amplitude maps of the myelin bilayer component do not provide differentiation between partly remyelinated and partly demyelinated tissue. Consequently, intermediate myelin amplitudes in and around MS lesions should be interpreted with due care, although it is worth noting that longitudinal monitoring will likely eliminate any ambiguity.

Direct access to the myelin bilayer through nonaqueous proton MRI is technically challenging due to the extremely rapid decay of myelin bilayer signals; dedicated short-T_2 imaging methodology and high-performance hardware capable of detecting and spatially encoding the targeted signals before considerable signal decay, as employed in the present study, are necessary to achieve successful myelin bilayer imaging (*22*).

It is possible to avoid the difficulties associated with the rapid decay of myelin bilayer signals by exploiting myelin-related properties of water signals to achieve myelin imaging with standard MRI systems (*23*, *24*). In a technique known as myelin water imaging (*25*), signals from the water trapped between the layers of lipid-protein bilayers in the myelin sheath are separated from signals stemming from water outside the myelin sheath through T_2 differences between the two water pools. The ratio of myelin water to nonmyelin water is used as a metric to quantify myelin content. Approaches based on the transfer of magnetization between macromolecules and water molecules are also common; of particular interest for myelin imaging is the inhomogeneous magnetization transfer imaging technique (*26*), which is believed to offer higher specificity for myelin than traditional magnetization transfer imaging techniques. That said, the arguably indirect nature of techniques based on the detection of water signals could limit their achievable myelin specificity compared to techniques directly accessing myelin bilayer signals.

Other noninvasive myelin imaging methods have been developed; among them are small angle x-ray scattering tensor tomography (*27*), positron emission tomography (*28*), and optical imaging (*29*). However, these methods rely on either ionizing radiation or the use of radiotracers or fluorescent probes, which renders their application in clinical practice more hazardous than MRI.

Based on the high myelin specificity achieved in both nonpathological (*17*) and MS brain tissue and the reasonable quality of the myelin bilayer maps in tissue with native water content, we consider our myelin bilayer mapping technique sufficiently validated for translation to in vivo application. Many of the limitations experienced ex vivo, such as strong susceptibility gradients, partial volume effects, and the potential lack of reliable reference NAWM regions for amplitude normalization, are not expected to transfer to the in vivo situation. That said, in vivo application introduces a previously unencountered set of technical challenges, the solutions to which will rely on the experiences gained ex vivo.

The myelin bilayer mapping procedure employed in this work uses the single-point imaging (SPI) (*30*) sequence to acquire the multi-echo MRI data used for model fitting (see Materials and Methods). The SPI sequence was chosen because, with each acquired image accurately reflecting the signal state at a specific point in time, it enables unbiased voxel-wise fitting and, hence, high confidence in the results. However, this feature comes at the cost of time efficiency, rendering SPI unsuitable for in vivo application.

Both the ultrashort echo time (UTE) (*31*) and the zero echo time (ZTE) (*32*) sequence designs offer more adequate time efficiency than SPI. UTE has been used in several myelin bilayer imaging studies (*33*–*41*), but, because the imaging gradient (whose amplitude determines the spatial encoding speed) is not ramped up until after tissue excitation, UTE is primarily sensitive to signals with T_2′s in the hundreds of microseconds range (*15*), whereas the vast majority of myelin bilayer signals exhibit T_2′s in the tens of microseconds range (*16*). As such, UTE images are considered to include only small contributions from the myelin bilayer. Consequently, translation of the myelin bilayer mapping technique to in vivo application will rather rely on the ZTE sequence, in which gradient ramping is performed before tissue excitation. That said, exploiting the spatial encoding speed advantage of ZTE for myelin bilayer imaging requires gradient hardware capable of reaching

and maintaining high amplitudes (hundreds of milliteslas per meter for human head); using standard gradient hardware (*20*, *42*, *43*), ZTE presents similarly limited sensitivity to myelin bilayer signals as UTE. Using the same custom-built, high-performance gradient hardware used in the present study, the ZTE variant with hybrid filling (HYFI) (*44*) has been shown to yield promising results for in vivo myelin bilayer imaging, albeit without separation of the two nonaqueous signal components (*16*). The suitability of ZTE data to replace SPI data in the model fitting procedure and, hence, the ability of ZTE data to yield quantitative, highly specific myelin bilayer maps require further investigation.

Noninvasive imaging of myelin is an unmet need in clinical practice and could benefit diagnostic workup of patients with MS as well as facilitate more personalized therapy, not least because the first remyelinating drugs are expected to be approved for MS therapy in the coming years. The myelin bilayer mapping technique pursued in this work holds the potential to fill this gap as MRI systems capable of short-T_2 imaging become increasingly available (*45*, *46*).

MATERIALS AND METHODS

Sample preparation

The MS tissue samples were provided by the U.K. MS Tissue Bank. Written informed consent was obtained by the MS donors or their next of kin, and the study was approved by the regional ethics review board. The brain samples had an average size of 25 mm by 21 mm by 4 mm, were freshly frozen upon retrieval at autopsy, and were subsequently stored at −80°C. In preparation for the MRI experiments, the samples were thawed and immersed in physiological saline solution (NaCl, 9 g/liter) of either H_2O or D_2O. For the samples placed in D_2O solution, the D_2O exchange was performed in two steps (i.e., the solution was refreshed once) over approximately 2 days. Consequently, the time interval between thawing the samples and the end of the imaging experiments was around 2 to 3 days for the D_2O samples, while only around half a day for the H_2O samples; when not undergoing imaging, the samples were stored at around 5°C. Imaging was performed with the samples at room temperature.

MRI experiments

Specialized imaging techniques and hardware are necessary to capture the extremely rapidly decaying signals from the myelin bilayer. A 3T Philips Achieva system (Philips Healthcare, The Netherlands) was used together with a high-performance insert gradient capable of gradient strength in excess of 200 mT/m at 100% duty cycle (*47*), a custom radiofrequency chain (*48*) including fast transmit/receive switches (*49*), and a ^{1}H-free transmit/receive loop coil of 40 mm diameter.

The imaging protocol used for model fitting consisted of 14 SPI images acquired at echo times (TEs) between 33 and 2000 μs with three-dimensional (3D) isotropic nominal resolution limited by maximum gradient strength to 1.56 mm. High-resolution (0.39 mm 3D isotropic) short-T_2 reference images were acquired using the HYFI sequence. Details on the imaging parameters for both protocols can be found in Table 3.

Model fitting

The employed signal model is complex and contains three components, each of which is defined by its amplitude (A), decay function [D_L for mono-exponential decay and D_{SL} for super-exponential decay (*50*, *51*)], decay constant (T_2 for mono-exponential decay and $T_{2,min}$ for super-exponential decay), and chemical shift (δ). In addition, the signal model contains an arbitrary phase offset (ϕ) and a local resonance frequency offset (Δf). Formally, the signal model is given by

$$S_{voxel}(t) = e^{i(\varphi+2\pi\Delta f t)}[A_U D_{SL}(T_{2,min,U}, t)e^{i2\pi\delta_U f_0 t} + A_S D_{SL}(T_{2,min,S}, t)e^{i2\pi\delta_S f_0 t} + A_W D_L(T_{2,W}, t)e^{i2\pi\delta_W f_0 t}]$$

where f_0 is the ^{1}H Larmor frequency.

Of the three signal components, two represent nonaqueous content and were characterized by super-exponential decay, and one represents aqueous content and was characterized by mono-exponential decay. The properties of the nonaqueous components used to define the signal model were determined in the reference study (*17*) for nonpathological WM: The most rapidly decaying nonaqueous component, referred to as the ultrashort (U) component and interpreted as representing the myelin bilayer (in WM), was described by a $T_{2,min}$ of 5.5 μs and a chemical shift of 1.1 parts per million (ppm). The other nonaqueous component, referred to as the short (S) component and interpreted as representing residual nonaqueous content, was described by a $T_{2,min}$ of 102 μs and a chemical shift of 2.1 ppm. The aqueous component, referred to as the water (W) component and interpreted as representing residual water content in D_2O samples and native water content in H_2O samples, was modeled as having a T_2 of 50 ms and a chemical shift of 4.7 ppm.

Least squares fitting to the multi-echo SPI images was used to determine the free parameters of the signal model, namely, the component amplitudes (A_U, A_S, and A_W), the global phase (not presented), and the local resonance frequency offset (Δf). Details on the algorithm can be found in the published analysis code (see Data and materials availability in Acknowledgements). Fitting was either performed on a voxel-by-voxel basis, thereby generating maps of the fitted parameters, or on signals averaged over multiple voxels in an ROI.

An alternative version of the signal model was also used for fitting, in which the decay constants ($T_{2,min,U}$ and $T_{2,min,S}$) and chemical shifts (not presented) of the two nonaqueous components

Table 3. Imaging parameters of the MRI protocols.

Protocol	Multi-echo	Reference
Sequence	SPI	HYFI
Field of view (mm)	50	50
Nominal resolution (mm)	1.56	0.39
Image bandwidth (kHz)	470–7.5	425
TE (μs)	33–2067	11
Excitation pulse	2 μs hard	2 μs hard
Repetition time (ms)	3	1
Scan time per image (m:s)	03:34	27:41

were also treated as free parameters. This fit was performed as a separate procedure because component amplitudes and decay constants are closely related parameters, so the component amplitudes are not comparable between fits if the component decay constants are determined simultaneously.

Data processing

For the H_2O samples, the two longest-TE images were discarded due to artifacts (*17*), so the longest TE was 827 μs.

Before model fitting, tricubic interpolation was performed on all SPI data to reduce the voxel size by a factor of two (in each dimension). The in-plane voxel size was reduced by a further factor of three for display purposes; this step was also performed for the HYFI reference images.

For H_2O samples, the myelin bilayer maps presented in Fig. 1 were manually masked on the basis of the sample outline seen in the water component map for the corresponding sample (equivalent to the A_W maps displayed in Fig. 3).

Histopathological processing

Subsequent to the MRI experiments, the samples were snap-frozen (−80°C) and cryosectioned into 10- to 20-μm-thick sections. The sections underwent immunohistochemistry for MOG (primary antibody concentration, 1:50) or myelin staining using LFB. For samples B1, C1, D2, and E1, the MOG sections were counterstained with hematoxylin. All LFB sections were counterstained with periodic acid–Schiff. Because of scarcity of tissue material, LFB staining could not be performed for all samples. All slides were scanned using a Hamamatsu slide scanner. Registration of the myelin bilayer amplitude maps with the processed tissue sections was performed manually.

Linear correlation analysis

Image intensities in corresponding tissue regions (within NAWM, NAGM, or the WM lesion) of the amplitude map of the ultrashort signal component representing the myelin bilayer (A_U) and the MOG stain were collected for sample A1 using ImageJ (National Institutes of Health, USA). The intensities were normalized so that the respective image background was at zero, and the maximum value was 100. Pearson's correlation coefficients were calculated in R (R Foundation for Statistical Computing, Austria) using the cor.test function.

Supplementary Materials

This PDF file includes:

Tables S1 and S2

REFERENCES AND NOTES

1. Multiple Sclerosis International Federation, *Atlas of MS, Part 1: Mapping Multiple Sclerosis Around the World: Key Epidemiology Findings* (ed. 3, 2020).
2. R. J. M. Franklin, M. Simons, CNS remyelination and inflammation: From basic mechanisms to therapeutic opportunities. *Neuron* **110**, 3549–3565 (2022).
3. R. M. Ransohoff, D. A. Hafler, C. F. Lucchinetti, Multiple sclerosis—A quiet revolution. *Nat. Rev. Neurol.* **11**, 134–142 (2015).
4. F. Piehl, Current and emerging disease-modulatory therapies and treatment targets for multiple sclerosis. *J. Intern. Med.* **289**, 771–791 (2021).
5. S. Faissner, J. R. Plemel, R. Gold, V. W. Yong, Progressive multiple sclerosis: From pathophysiology to therapeutic strategies. *Nat. Rev. Drug Discov.* **18**, 905–922 (2019).
6. C. Lubetzki, B. Zalc, A. Williams, C. Stadelmann, B. Stankoff, Remyelination in multiple sclerosis: From basic science to clinical translation. *Lancet Neurol.* **19**, 678–688 (2020).
7. M. P. Wattjes, O. Ciccarelli, D. S. Reich, B. Banwell, N. De Stefano, C. Enzinger, F. Fazekas, M. Filippi, J. Frederiksen, C. Gasperini, Y. Hacohen, L. Kappos, D. K. B. Li, K. Mankad, X. Montalban, S. D. Newsome, J. Oh, J. Palace, M. A. Rocca, J. Sastre-Garriga, M. Tintoré, A. Traboulsee, H. Vrenken, T. Yousry, F. Barkhof, À. Rovira, M. P. Wattjes, O. Ciccarelli, N. De Stefano, C. Enzinger, F. Fazekas, M. Filippi, J. Frederiksen, C. Gasperini, Y. Hacohen, L. Kappos, K. Mankad, X. Montalban, J. Palace, M. A. Rocca, J. Sastre-Garriga, M. Tintore, H. Vrenken, T. Yousry, F. Barkhof, A. Rovira, D. K. B. Li, A. Traboulsee, S. D. Newsome, B. Banwell, J. Oh, D. S. Reich, D. S. Reich, J. Oh, 2021 MAGNIMS–CMSC–NAIMS consensus recommendations on the use of MRI in patients with multiple sclerosis. *Lancet Neurol.* **20**, 653–670 (2021).
8. B. V. Ineichen, E. S. Beck, M. Piccirelli, D. S. Reich, New prospects for ultra-high-field magnetic resonance imaging in multiple sclerosis. *Invest. Radiol.* **56**, 773–784 (2021).
9. M. Filippi, W. Brück, D. Chard, F. Fazekas, J. J. G. Geurts, C. Enzinger, S. Hametner, T. Kuhlmann, P. Preziosa, À. Rovira, K. Schmierer, C. Stadelmann, M. A. Rocca, Association between pathological and MRI findings in multiple sclerosis. *Lancet Neurol.* **18**, 198–210 (2019).
10. S. G. Waxman, L. Bangalore, "Electrophysiologic consequences of myelination" in *Myelin biology and Disorders* (Elsevier, 2004), chap. 5.
11. M. N. Rasband, W. B. Macklin, "Myelin structure and biochemistry" in *Basic Neurochemistry*, S. T. Brady, G. J. Siegel, R. W. Albers, D. L. Price, Eds. (Elsevier, 2012), chap. 10, pp. 180–199.
12. C. Stadelmann, S. Timmler, A. Barrantes-Freer, M. Simons, Myelin in the central nervous system: Structure, function, and pathology. *Physiol. Rev.* **99**, 1381–1431 (2019).
13. A. L. MacKay, C. Laule, Magnetic resonance of myelin water: An in vivo marker for myelin. *Brain Plast.* **2**, 71–91 (2016).
14. M. J. Wilhelm, H. H. Ong, S. L. Wehrli, C. Li, P. H. Tsai, D. B. Hackney, F. W. Wehrli, Direct magnetic resonance detection of myelin and prospects for quantitative imaging of myelin density. *Proc. Natl. Acad. Sci. U.S.A.* **109**, 9605–9610 (2012).
15. R. Froidevaux, M. Weiger, M. B. Rösler, D. O. Brunner, B. E. Dietrich, J. Reber, K. P. Pruessmann, High-resolution short-T_2 MRI using a high-performance gradient. *Magn. Reson. Med.* **84**, 1933–1946 (2020).
16. M. Weiger, R. Froidevaux, E. L. Baadsvik, D. O. Brunner, M. B. Rösler, K. P. Pruessmann, Advances in MRI of the myelin bilayer. *Neuroimage* **217**, 116888 (2020).
17. E. L. Baadsvik, M. Weiger, R. Froidevaux, W. Faigle, B. V. Ineichen, K. P. Pruessmann, Mapping the myelin bilayer withshort-T_2 MRI: Methods validation and reference data for healthy human brain. *Magn. Reson. Med.* **89**, 665–677 (2023).
18. N. M. Moll, A. M. Rietsch, S. Thomas, A. J. Ransohoff, J.-C. Lee, R. Fox, A. Chang, R. M. Ransohoff, E. Fisher, Multiple sclerosis normal-appearing white matter: Pathology-imaging correlations. *Ann. Neurol.* **70**, 764–773 (2011).
19. R. A. Horch, J. C. Gore, M. D. Does, Origins of the ultrashort-T_2 ^{1}H NMR signals in myelinated nerve: A direct measure of myelin content? *Magn. Reson. Med.* **66**, 24–31 (2011).
20. A. C. Seifert, C. Li, M. J. Wilhelm, S. L. Wehrli, F. W. Wehrli, Towards quantification of myelin by solid-state MRI of the lipid matrix protons. *Neuroimage* **163**, 358–367 (2017).
21. A. P. Manning, A. L. Mackay, C. A. Michal, Understanding aqueous and non-aqueous proton T1 relaxation in brain. *J. Magn. Reson.* **323**, 106909 (2021).
22. M. Weiger, K. P. Pruessmann, Short-T_2 MRI: Principles and recent advances. *Prog. Nucl. Magn. Reson. Spectrosc.* **114-115**, 237–270 (2019).
23. C. Laule, I. M. Vavasour, S. H. Kolind, D. K. B. Li, T. L. Traboulsee, G. R. W. Moore, A. L. MacKay, Magnetic resonance imaging of myelin. *Neurotherapeutics* **4**, 460–484 (2007).
24. G. F. Piredda, T. Hilbert, J. P. Thiran, T. Kober, Probing myelin content of the human brain with MRI: A review. *Magn. Reson. Med.* **85**, 627–652 (2021).
25. A. MacKay, K. Whittall, J. Adler, D. Li, D. Paty, D. Graeb, In vivo visualization of myelin water in brain by magnetic resonance. *Magn. Reson. Med.* **31**, 673–677 (1994).
26. G. Varma, G. Duhamel, C. de Bazelaire, D. C. Alsop, Magnetization transfer from inhomogeneously broadened lines: A potential marker for myelin. *Magn. Reson. Med.* **73**, 614–622 (2015).
27. M. Georgiadis, A. Schroeter, Z. Gao, M. Guizar-Sicairos, M. Liebi, C. Leuze, J. A. McNab, A. Balolia, J. Veraart, B. Ades-Aron, S. Kim, T. Shepherd, C. H. Lee, P. Walczak, S. Chodankar, P. Digiacomo, G. David, M. Augath, V. Zerbi, S. Sommer, I. Rajkovic, T. Weiss, O. Bunk, L. Yang, J. Zhang, D. S. Novikov, M. Zeineh, E. Fieremans, M. Rudin, Nanostructure-specific X-ray tomography reveals myelin levels, integrity and axon orientations in mouse and human nervous tissue. *Nat. Commun.* **12**, 2941 (2021).
28. B. Stankoff, Y. Wang, M. Bottlaender, M.-S. Aigrot, F. Dolle, C. Wu, D. Feinstein, G.-F. Huang, F. Semah, C. A. Mathis, Imaging of CNS myelin by positron-emission tomography. *Proc. Natl. Acad. Sci. U.S.A.* **103**, 9304–9309 (2006).
29. C. Wang, C. Wu, D. C. Popescu, J. Zhu, W. B. Macklin, R. H. Miller, Y. Wang, Longitudinal near-infrared imaging of myelination. *J. Neurosci.* **31**, 2382–2390 (2011).

30. B. J. Balcom, R. P. MacGregor, S. D. Beyea, D. P. Green, R. L. Armstrong, T. W. Bremner, Single-point ramped imaging with T_1 enhancement (SPRITE). *J. Magn. Reson. Ser. A* **123**, 131–134 (1996).
31. J. E. Holmes, G. M. Bydder, MR imaging with ultrashort TE (UTE) pulse sequences: Basic principles. *Radiography* **11**, 163–174 (2005).
32. M. Weiger, K. P. Pruessmann, "MRI with zero echo time" in *eMagRes* (John Wiley & Sons, 2012), vol. 1, pp. 311–322.
33. K. S. Nayak, J. M. Pauly, G. E. Gold, D. G. Nishimura, imaging ultra-short T_2 species in the brain, in *Proceedings of the ISMRM 8th Scientific Meeting & Exhibition*, Denver, USA, 2000, p. 509.
34. E. Ercan, P. Boernert, A. Webb, I. Ronen, Whole-brain tissue-based assessment of the ultrashort T_2 component using 3D UTE MRI relaxometry, in *Proceedings of the ISMRM 20th Annual Meeting & Exhibition*, Melbourne, Australia, 2012, p. 4279.
35. J. Du, G. Ma, S. Li, M. Carl, N. M. Szeverenyi, S. VandenBerg, J. Corey-Bloom, G. M. Bydder, Ultrashort echo time (UTE) magnetic resonance imaging of the short T_2 components in white matter of the brain using a clinical 3T scanner. *Neuroimage* **87**, 32–41 (2014).
36. V. Sheth, H. Shao, J. Chen, S. Vandenberg, J. Corey-Bloom, G. M. Bydder, J. Du, Magnetic resonance imaging of myelin using ultrashort Echo time (UTE) pulse sequences: Phantom, specimen, volunteer and multiple sclerosis patient studies. *Neuroimage* **136**, 37–44 (2016).
37. S. J. Fan, Y. Ma, Y. Zhu, A. Searleman, N. M. Szeverenyi, G. M. Bydder, J. Du, Yet more evidence that myelin protons can be directly imaged with UTE sequences on a clinical 3T scanner: Bicomponent T_2^* analysis of native and deuterated ovine brain specimens. *Magn. Reson. Med.* **80**, 538–547 (2018).
38. Y. J. Ma, A. C. Searleman, H. Jang, S. J. Fan, J. Wong, Y. Xue, Z. Cai, E. Y. Chang, J. Corey-Bloom, J. Du, Volumetric imaging of myelin in vivo using 3D inversion recovery-prepared ultrashort echo time cones magnetic resonance imaging. *NMR Biomed.* **33**, e4326 (2020).
39. Y.-J. Ma, H. Jang, Z. Wei, Z. Cai, Y. Xue, R. R. Lee, E. Y. Chang, G. M. Bydder, J. Corey-Bloom, J. Du, Myelin imaging in human brain using a short repetition time adiabatic inversion recovery prepared ultrashort echo time (STAIR-UTE) MRI sequence in multiple sclerosis. *Radiology* **297**, 392–404 (2020).
40. M. Muller, N. Egger, S. Sommer, T. Wilferth, C. R. Meixner, F. B. Laun, A. Mennecke, M. Schmidt, K. Huhn, V. Rothhammer, M. Uder, A. Dorfler, A. M. Nagel, Direct imaging of white matter ultrashort T_2^* components at 7 Tesla. *Magn. Reson. Imag.* **86**, 107–117 (2022).
41. X. Shen, A. C. Özen, A. Sunjar, S. Ilbey, S. Sawiak, R. Shi, M. Chiew, U. Emir, Ultra-short T_2 components imaging of the whole brain using 3D dual-echo UTE MRI with rosette k-space pattern. *Magn. Reson. Med.* **89**, 508–521 (2023).
42. A. C. Seifert, M. Umphlett, M. Hefti, M. Fowkes, J. Xu, Formalin tissue fixation biases myelin-sensitive MRI. *Magn. Reson. Med.* **82**, 1504–1517 (2019).
43. H. Jang, M. Carl, Y. Ma, A. C. Searleman, S. Jerban, E. Y. Chang, J. Corey-Bloom, J. Du, Inversion recovery zero echo time (IR-ZTE) imaging for direct myelin detection in human brain: A feasibility study. *Quant. Imaging Med. Surg.* **10**, 895–906 (2020).
44. R. Froidevaux, M. Weiger, M. B. Rosler, D. O. Brunner, K. P. Pruessmann, HYFI: Hybrid filling of the dead-time gap for faster zero echo time imaging. *NMR Biomed.* **34**, e4493 (2021).
45. T. K. F. Foo, M. Vermilyea, M. Xu, A. Wu, Y. Hua, W. Stautner, Y. Bai, J. Ricci, D. Kelley, J. I. Huston, Y. Shu, M. A. Bernstein, C. Hess, D. Xu, Design and construction of a low-cryogen, lightweight, high-performance, head-only compact 7T MRI, in *Proceedings of the ISMRM & SMRT Annual Meeting & Exhibition*, 2021, p. 0561.
46. D. A. Feinberg, P. Dietz, C. Liu, K. Setsompop, P. Mukherjee, L. L. Wald, A. T. Vu, A. J. Beckett, I. G. Insua, M. Schröder, S. Stocker, P. H. Bell, E. Rummert, M. Davids, Design and development of a next-generation 7T human brain scanner with high-performance gradient coil and dense RF arrays, in *Proceedings of the ISMRM & SMRT Annual Meeting & Exhibition*, 2021, p. 0562.
47. M. Weiger, J. Overweg, M. B. Rösler, R. Froidevaux, F. Hennel, B. J. Wilm, A. Penn, U. Sturzenegger, W. Schuth, M. Mathlener, M. Borgo, P. Börnert, C. Leussler, R. Luechinger, B. E. Dietrich, J. Reber, D. O. Brunner, T. Schmid, L. Vionnet, K. P. Pruessmann, A high-performance gradient insert for rapid and short-T_2 imaging at full duty cycle. *Magn. Reson. Med.* **79**, 3256–3266 (2018).
48. B. E. Dietrich, D. O. Brunner, B. J. Wilm, C. Barmet, S. Gross, L. Kasper, M. Haeberlin, T. Schmid, S. J. Vannesjo, K. P. Pruessmann, A field camera for MR sequence monitoring and system analysis. *Magn. Reson. Med.* **75**, 1831–1840 (2016).
49. D. O. Brunner, L. Furrer, M. Weiger, W. Baumberger, T. Schmid, J. Reber, B. E. Dietrich, B. J. Wilm, R. Froidevaux, K. P. Pruessmann, Symmetrically biased T/R switches for NMR and MRI with microsecond dead time. *J. Magn. Reson.* **263**, 147–155 (2016).
50. H. Wennerström, Proton nuclear magnetic resonance lineshapes in lamellar liquid crystals. *Chem. Phys. Lett.* **18**, 41–44 (1973).
51. M. Bloom, E. E. Burnell, M. I. Valic, G. Weeks, Nuclear magnetic resonance line shapes in lipid bi-layer model membranes. *Chem. Phys. Lipids* **14**, 107–112 (1975).

Acknowledgments: We would like to thank R. Reynolds from the U.K. MS Tissue Bank for providing brain samples from patients with MS and MOG antibody for immunohistochemical processing. **Author contributions:** Conceptualization: E.L.B., M.W., R.F., and K.P.P. Methodology: E.L.B., M.W., R.F., W.F., and B.V.I. Resources: M.W., W.F., B.V.I., and K.P.P. Investigation: E.L.B. and M.W. Visualization: E.L.B. Formal analysis: E.L.B. Software: E.L.B., M.W., and R.F. Supervision: B.V.I. and K.P.P. Writing—original draft: E.L.B. Writing—review and editing: M.W., B.V.I., and K.P.P. **Competing interests:** K.P.P. holds a research agreement with and receives research support from Philips and is a shareholder of GyroTools LLC. All other authors declare that they have no competing interests. **Data and materials availability:** All data needed to evaluate the conclusions in the paper are present in the paper and/or the Supplementary Materials or can be downloaded from the ETH Research Collection at https://doi.org/10.3929/ethz-b-000615057. The same MRI processing pipeline as used in the reference study (*17*) was used; see this publication for analysis code.

Submitted 31 March 2023
Accepted 7 July 2023
Published 11 August 2023
10.1126/sciadv.adi0611

ScienceAdvances

Quantitative magnetic resonance mapping of the myelin bilayer reflects pathology in multiple sclerosis brain tissue

Emily Louise Baadsvik, Markus Weiger, Romain Froidevaux, Wolfgang Faigle, Benjamin V. Ineichen, and Klaas P. Pruessmann

Sci. Adv. **9** (32), eadi0611. DOI: 10.1126/sciadv.adi0611